

# A Novel Implementation of the Matrix Element Method at Next-to-Leading Order for the Measurement of the Higgs Self-Coupling $\lambda_{3H}$

Matthias Tartarin<sup>1,\*</sup> and Jan Stark<sup>1,†</sup>

<sup>1</sup>Université de Toulouse, CNRS/IN2P3, L2IT, Toulouse, France

(Dated: February 3, 2026)

The determination of the Higgs boson trilinear self-coupling  $\lambda_{3H}$  is a key goal of the LHC physics programme. Its precise measurement will provide unique insight into the scalar potential and the mechanism of electroweak symmetry breaking. Higgs boson pair production in the  $gg \rightarrow HH$  process, and particularly in the  $HH \rightarrow b\bar{b}\gamma\gamma$  final state, offers direct sensitivity to  $\lambda_{3H}$ .

We present the first implementation of the Matrix Element Method at Next-to-Leading Order (MEM@NLO) for this process, which is publicly available. The MEM is a statistically optimal approach that maximises information extraction from collision events. Extending it to NLO represents a major methodological challenge, which we address with a new formalism integrated into the MoMEMTA framework. Results with simulated pseudo-experiments demonstrate, in a proof-of-principle study, the strong discriminating power of the method and its ability to extract the coupling modifier  $\kappa_\lambda = \lambda_{3H}/\lambda_{3H}^{SM}$  with high precision.

## I. INTRODUCTION

The discovery of the Higgs boson in 2012 [1, 2] at the Large Hadron Collider (LHC) by the ATLAS [3] and CMS [4] collaborations completed the experimental confirmation of the Standard Model (SM) particle content. Despite this milestone, the form of the Higgs potential itself remains only weakly constrained experimentally. As the leading self-interaction of the Higgs sector, the trilinear Higgs self-coupling  $\lambda_{3H}$  is particularly sensitive to modifications of the Higgs potential, and therefore provides a powerful probe of the Higgs sector, and possible new dynamics beyond the Standard Model.

Such deviations can affect both the total rate and the event-level kinematics of Higgs boson pair production, which makes  $\lambda_{3H}$  a key target of the LHC physics programme and its future phases (such as the High-Luminosity LHC, HL-LHC) [5, 6]. In a broader class of scenarios, such modifications may also play a crucial role in explaining the observed matter-antimatter asymmetry of the Universe [7].

Despite extensive searches, di-Higgs production has not yet been observed at the LHC. The current limits on  $\lambda_{3H}$  (often expressed via the coupling modifier  $\kappa_\lambda = \lambda_{3H}/\lambda_{3H}^{SM}$ ) still allow sizeable deviations from the SM prediction. Using the full Run 2 dataset, ATLAS and CMS have performed combined interpretations of the major di-Higgs channels (with final states  $b\bar{b}b\bar{b}$ ,  $b\bar{b}\tau^+\tau^-$ ,  $b\bar{b}\gamma\gamma$ , and multileptons), yielding constraints at 95% confidence level of  $-1.2 < \kappa_\lambda < 7.2$  from ATLAS [8] and  $-1.4 < \kappa_\lambda < 7.0$  from CMS [9].

The most recent ATLAS analysis in the  $b\bar{b}\gamma\gamma$  final state, combining Run 2 and early Run 3 data (corresponding to

a total integrated luminosity of  $308 \text{ fb}^{-1}$ ), sets limits on the coupling modifier  $-1.4 < \kappa_\lambda < 6.8$  at 95% CL [10], representing the most stringent constraints obtained to date in this channel. While increased luminosity is a necessary ingredient to improve statistical precision on measurements, it is not sufficient alone. Fully exploiting the available data also requires analysis techniques capable of extracting the maximal discriminating power from event-level kinematics.

The Matrix Element Method (MEM) [11, 12] provides a natural framework to address this challenge. By exploiting the full event-level kinematic information through first-principles likelihoods, it is particularly well suited to the extraction of parameters associated with rare processes. The MEM has been successfully applied to measurements with limited statistics and significant background, most notably for the determination of the top quark mass at the Tevatron [13–15].

The measurement of Higgs boson pair production at the LHC presents closely analogous challenges, as the extraction of the Higgs self-coupling  $\lambda_{3H}$  relies on a process with very small production rates and limited statistical sensitivity. However, most existing applications of the MEM rely on Leading-Order (LO) matrix elements, neglecting higher-order QCD radiation. As a result, LO-based MEM analyses suffer from reduced accuracy when applied to realistic LHC events, motivating the development of strategies to incorporate next-to-leading order (NLO) QCD effects within MEM-based frameworks [16–19].

The strategy presented in this work introduces a new framework and realises the first MEM at Next-to-Leading Order (NLO) [20] for the process  $gg \rightarrow HH \rightarrow b\bar{b}\gamma\gamma$ , enabling a precise and robust extraction of  $\kappa_\lambda$  for realistic events. This study follows up on the results at LO only, reported in Ref. [21].

\* matthias.tartarin@l2it.in2p3.fr

† jan.stark@l2it.in2p3.fr

## II. THE MATRIX ELEMENT METHOD

The Matrix Element Method (MEM) provides a statistically optimal way to exploit the full kinematic information from collision events, by evaluating the likelihood that a measured event with reconstructed observables  $\mathbf{x}^i$  originates from a given process  $p$  under a set of model hypotheses  $\mathbf{h}$ .

Each process  $p$  corresponds to a specific hard-scattering topology, and is characterised by parameters  $\mathbf{h}$  such as the coupling modifier  $\kappa_\lambda$ . The relevant signal process for this analysis is gluon-fusion ( $ggF$ ) di-Higgs production  $gg \rightarrow HH \rightarrow b\bar{b}\gamma\gamma$ , while the main background processes include  $t\bar{t}H$ , QCD-induced diphoton production, and single-Higgs (plus-jets) production.

For a given event  $i$ , the reconstructed quantities  $\mathbf{x}^i$  denote the four-momenta of the observed final-state objects. The MEM then integrates over all parton-level four-momenta  $\mathbf{y}$  that are compatible with these reconstructed measurements. From first principles, the corresponding process likelihood for event  $i$  can be expressed as:

$$\begin{aligned} \mathcal{L}_{\text{process}}^p(\mathbf{h}|\mathbf{x}^i) &= \frac{(2\pi)^4}{\sigma_p^{\text{obs}}(pp \rightarrow F)} \int_{\mathbf{y}} \int_{q_1, q_2} \sum_{a_1, a_2} f_{a_1}(q_1) f_{a_2}(q_2) \\ &\quad \times \frac{|\mathcal{M}_p(a_1 a_2 \rightarrow \mathbf{y}; \mathbf{h})|^2}{q_1 q_2 s} W(\mathbf{y}, \mathbf{x}^i) \\ &\quad \times \delta(a_1 + a_2 - \sum_{j=1}^n y_j) dq_1 dq_2 d^{4n} \mathbf{y}, \end{aligned} \quad (1)$$

where the various quantities entering Eq. (1) are:

- $\sigma_p^{\text{obs}}(pp \rightarrow F)$  which corresponds to the observable integrated cross section (*i.e.* the fiducial cross section multiplied by the detector efficiency) to produce the final-state partons  $F$  for the process  $p$ , used to normalise the likelihood;
- $q_1$  and  $q_2$  are the momentum fractions of partons  $a_1$  and  $a_2$  (also referred to as Bjorken- $x$  scaling variables), and  $s$  is the Mandelstam variable corresponding to the squared centre-of-mass energy of the proton-proton collision;
- $\mathcal{M}_p(a_1 a_2 \rightarrow \mathbf{y}; \mathbf{h})$  denotes the partonic matrix element of  $a_1 a_2 \rightarrow \mathbf{y}$  for the process  $p$  and the hypothesis  $\mathbf{h}$ , obtained from first principles in quantum field theory;
- $\delta^{(4)}(a_1 + a_2 - \sum_j y_j)$  are  $\delta$ -functions that enforce energy-momentum conservation;
- $W(\mathbf{y}, \mathbf{x}^i)$  corresponds to the transfer functions, which parameterise the detector response and describe the probability for a parton-level configuration  $\mathbf{y}$  to give rise to the reconstructed observables  $\mathbf{x}^i$ .

MoMEMTA [22] is a modular framework designed to implement the MEM in high-energy physics analyses through numerical evaluation of the integral in Eq. (1). It provides a flexible environment in which the ingredients of the MEM integrand are defined and handled as separate *modules*. Yet, because the MEM involves integrations over a high-dimensional phase space, the numerical complexity can quickly become very challenging. To make these calculations more manageable, MoMEMTA uses dedicated modules called *blocks* that perform analytic changes of variables using kinematic constraints (*e.g.* from intermediate resonances such as the Higgs boson) and conservation laws encoded in the  $\delta$ -functions to reduce the dimensionality of the integration.

At LO, the MoMEMTA modular approach performs remarkably well, as the phase space has a simple structure and the mapping between partonic and reconstructed objects is straightforward.

At NLO however, additional complications arise. While virtual corrections preserve the LO final-state topology, real-emission contributions introduce an extra parton and therefore a different phase space configuration. For this analysis, the extra radiation will be treated as unresolved (*i.e.* no attempt is made to reconstruct the additional parton in the detector) and will be fully integrated over. This allows all NLO contributions to be consistently mapped onto the LO-like final-state  $\mathbf{x}^i$ , corresponding to the kinematics of reconstructed  $b\bar{b}\gamma\gamma$  event.

## III. ACCESSING THE MATRIX ELEMENTS AT NLO

At NLO, the differential cross section separates into three contributions:

$$d\sigma_{\text{NLO}} = \underbrace{[B(\Phi_n) + V(\Phi_n)] d\Phi_n}_{\text{Born+Virtual}} + \underbrace{R(\Phi_{n+1}) d\Phi_{n+1}}_{\text{Real}}, \quad (2)$$

where  $B$  denotes the Born (or LO) contribution,  $V$  the virtual loop correction with the same final-state multiplicity, and  $R$  the real-emission matrix element with one additional parton.

The cancellation of soft and collinear singularities between the virtual and real contributions must be treated consistently to ensure that the separate Born+Virtual and Real-emission terms remain finite and numerically stable. As discussed in the following subsections, our framework interfaces the MEM integrand directly with these finite, regularised NLO matrix element contributions on a point-by-point basis, enabling the explicit construction of the likelihood while preserving infrared safety and numerical stability across the entire phase space.

### Virtual vs. Real: practical challenges.

As one can see from Eq. (2), virtual contributions share the same kinematic topology as the Born term and can, in principle, be evaluated over the same  $d\Phi_n$  phase space. However, they contain infrared poles and depend on specific conventions and must be handled consistently to ensure numerical stability and proper matching with the real-emission component.

Real emission, in contrast, lives in the  $d\Phi_{n+1}$  phase-space and introduces an extra parton and integration variables. In the MEM framework, this additional radiation does not need to be explicitly reconstructed at detector level. Instead, it can be consistently accounted for by integrating over its corresponding extra three degrees of freedom. This requires a careful treatment of the soft and collinear regions to maintain infrared safety and numerical stability in the MEM.

### Strategy: repurposing POWHEG-BOX-V2 to access pointwise matrix elements.

Computing the likelihood  $\mathcal{L}_{\text{process}}^p(\mathbf{h}|\mathbf{x}^i)$  requires access to the matrix element  $\mathcal{M}_p$ , evaluated at specific phase-space points. At NLO, this involves going beyond the leading Born term by including both virtual loop corrections and real-emission contributions.

To obtain pointwise access to the amplitudes at arbitrary phase-space points, we use the POWHEG-BOX-V2 software [23], and in particular its dedicated ggHH subrepository developed by Heinrich *et al.* [24, 25]. This implementation provides configurable  $\kappa_\lambda$  and top-mass schemes.

POWHEG-BOX-V2 is a general NLO Monte Carlo framework designed for the computation of cross sections and the generation of fully exclusive events at NLO accuracy, with subsequent parton-showering provided via its interface to PYTHIA [26].

By construction, POWHEG-BOX-V2 does not natively provide external access to the individual Born, Virtual, and Real contributions at arbitrary phase-space points. A central part of this work therefore consisted in adapting the internal routines of POWHEG-BOX-V2 and developing a dedicated interface to MoMEMTA, enabling point-by-point access to these amplitudes for user-specified phase-space configurations. Accessing each of them is required for the explicit evaluation of the matrix element entering the likelihood defined in Eq. (1). This interface between the two softwares is a key component of this new MEM@NLO implementation, and a detailed description of its structure and the validation procedures are given in Ref. [20].

To promote open access and ensure reproducibility of our results, a public version of this study, together with additional auxiliary material, is provided in Ref. [27].

### IV. INTERFACING TO MOMEMTA.

As mentioned earlier, real-emission contributions at NLO introduce an additional parton in the final state, modifying both the dimensionality and structure of the phase-space integration, even when the emitted radiation is treated as unresolved.

The MoMEMTA framework, originally designed for LO implementations of the MEM, does not include any block capable of handling the integration of real NLO contributions. To overcome this limitation, we developed a new component, BLOCK N.

#### New Block N: Design and principle

Blocks in MoMEMTA are used to reduce the dimensionality of the integral in Eq. (1) through well-chosen changes of variables. Building on a systematic study of all existing blocks and their Jacobians, we developed a new block that we called BLOCK N, specifically designed to incorporate the additional degrees of freedom related to the unresolved real emissions at NLO.

A graphical representation of this new BLOCK N is shown in Fig. 1.

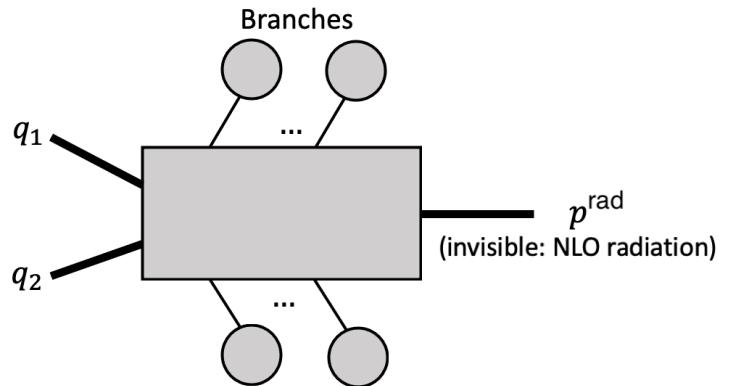


FIG. 1: Schematic representation of the new BLOCK N, following the conventions used by MoMEMTA.

The design principle of the new BLOCK N is to simultaneously eliminate the two Bjorken- $x$  fractions ( $q_1, q_2$ ) and the transverse components of the radiated parton momentum ( $p_x^{\text{rad}}, p_y^{\text{rad}}$ ) using four-momentum conservation, while keeping its longitudinal component  $p_z^{\text{rad}}$  as a free integration variable.

The choice to keep  $p_z^{\text{rad}}$  is also motivated by physical considerations: its direction coincides with the unknown net boost of the system of the two initial-state partons, along the beam axis, which cannot be reconstructed from the final state alone.

The corresponding Jacobian associated to the BLOCK N is derived from the system:

$$\begin{cases} p_x^{\text{rad}} = -P_x, \\ p_y^{\text{rad}} = -P_y, \\ q_{1,E} - q_{2,E} = P_z, \\ q_{1,E} + q_{2,E} - \sqrt{(p_x^{\text{rad}})^2 + (p_y^{\text{rad}})^2 + (p_z^{\text{rad}})^2} = E_T, \end{cases}$$

where  $P_x$ ,  $P_y$ ,  $P_z$  and  $E_T$  are the sums of the corresponding contributions over final-state  $b\bar{b}\gamma\gamma$ ,  $p^{\text{rad}}$  denotes the unresolved real-radiation, and  $q_{i,E} = \frac{1}{\sqrt{2}}q_i\sqrt{s}$  is the energy of gluon  $i$ .

From this system of equations, we can compute the Jacobian associated with the change of variables:

$$\begin{aligned} J^{-1} &= \begin{pmatrix} \frac{\partial P_x}{\partial p_x^{\text{rad}}} & \frac{\partial P_x}{\partial p_y^{\text{rad}}} & \frac{\partial P_x}{\partial q_{1,E}} & \frac{\partial P_x}{\partial q_{2,E}} \\ \frac{\partial P_y}{\partial p_x^{\text{rad}}} & \frac{\partial P_y}{\partial p_y^{\text{rad}}} & \frac{\partial P_y}{\partial q_{1,E}} & \frac{\partial P_y}{\partial q_{2,E}} \\ \frac{\partial P_z}{\partial p_x^{\text{rad}}} & \frac{\partial P_z}{\partial p_y^{\text{rad}}} & \frac{\partial P_z}{\partial q_{1,E}} & \frac{\partial P_z}{\partial q_{2,E}} \\ \frac{\partial E_T}{\partial p_x^{\text{rad}}} & \frac{\partial E_T}{\partial p_y^{\text{rad}}} & \frac{\partial E_T}{\partial q_{1,E}} & \frac{\partial E_T}{\partial q_{2,E}} \end{pmatrix} \\ &= \begin{pmatrix} -1 & 0 & 0 & 0 \\ 0 & -1 & 0 & 0 \\ 0 & 0 & 1 & -1 \\ -\frac{p_x^{\text{rad}}}{E^{\text{rad}}} & -\frac{p_y^{\text{rad}}}{E^{\text{rad}}} & 1 & 1 \end{pmatrix}. \end{aligned} \quad (3)$$

The determinant of the inverse Jacobian matrix  $J^{-1}$  reads:

$$\begin{aligned} |\det(J^{-1})| &= \left| (-1)(-1) \cdot \det \begin{pmatrix} 1 & -1 \\ 1 & 1 \end{pmatrix} \right| \\ &= \left| \det \begin{pmatrix} 1 & -1 \\ 1 & 1 \end{pmatrix} \right| = |2| = 2, \end{aligned} \quad (4)$$

and the determinant that needs to be implemented in the code for BLOCK N is:

$$|\det(J)| = \frac{1}{|\det(J^{-1})|} = \frac{1}{2}. \quad (5)$$

### Validation of Block N

Given the novelty of the Block N construction, a dedicated validation strategy was required to ensure the correctness of the phase-space transformation and its associated Jacobian.

A detailed description of this procedure, together with the associated figures demonstrating the consistency of the Block N implementation, is provided in Appendix A.

### Infrared safety and stability

A well-known feature of QCD perturbative calculations at fixed order is singularities in the soft and collinear limits for real emission matrix elements.

In our implementation, this cancellation is handled at the level of the matrix elements provided by

POWHEG-BOX-V2, which we modified to supply finite, infrared-safe Born+virtual and real-emission contributions at each phase-space point. Nevertheless, embedding these ingredients into a fully differential, multidimensional MEM integration requires additional care from a numerical point of view.

To ensure stable and efficient numerical convergence of the MEM integral, we impose a minimal transverse-momentum threshold on the additional radiated parton within the integration. This requirement does not constitute a subtraction of infrared singularities nor a modification of the underlying NLO prediction, but serves as a technical regulator to avoid regions of phase space that lead to inefficient sampling.

### Collinear treatment module

In addition to the transverse-momentum cut-off, a dedicated collinear treatment module is implemented to regulate configurations in which the radiated parton becomes nearly parallel to an incoming gluon or one of the Higgs decay products. In this collinear limit, the real-radiation four-momentum, together with that of the collinear particle, is locally redefined to reflect how the detector would reconstruct only the decay product. This procedure also ensures smooth numerical behaviour of the MEM integrand across the singular regions.

## V. VALIDATION AND DISCRIMINATION POWER

The separation power of the MEM@NLO is most directly illustrated with rejection curves (ROC curves), built from the event-by-event likelihood ratio between the signal and a chosen background hypothesis. The efficiency of a given cut on this discriminant is evaluated using simulated samples of signal (horizontal axis) and background (vertical axis) events. For this analysis, the likelihoods are computed from Eq. (1) using the MEM.

The comparison in Fig. 2 highlights the necessity of extending the MEM to NLO accuracy. The MEM@LO has its sensitivity degrading significantly on realistic NLO samples as it does not account for the extra radiation. In contrast, the MEM@NLO achieves and restores an improved discrimination power on NLO events, thanks to its more realistic description of the underlying physics.

Beyond the ROC performances, additional cross-checks were performed to validate the numerical accuracy of the MEM@NLO implementation and its many interfaces. The LO and real-emission matrix elements obtained from POWHEG-BOX-V2 were compared with those from MADGRAPH5\_AMC@NLO [28] (another broadly used Monte Carlo generator), showing excellent agreement across representative phase-space points.

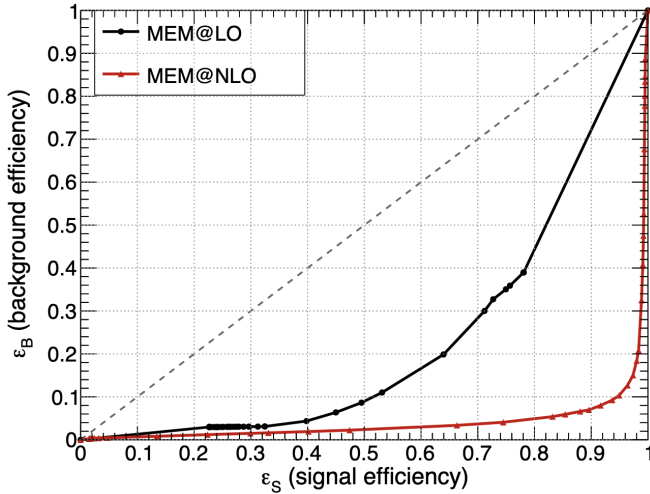


FIG. 2: ROC curve for events generated at NLO, between the  $ggF$  di-Higgs signal and  $ttH$  background. The black curve corresponds to MEM@LO, and the red curve to MEM@NLO. Given our conventions, the closer the ROC curve lies to the bottom-right corner of the plot, the more powerful the method.

## VI. EXTRACTION OF THE HIGGS SELF-COUPLING USING LIKELIHOOD SCANS

Beyond discrimination between the different processes  $p$ , the ultimate goal of the MEM@NLO is to extract the Higgs trilinear coupling  $\kappa_\lambda$ . To achieve this, one can define three likelihood functions:

- The *kinematic likelihood*,  $\mathcal{L}_{\text{kin}}(\kappa_\lambda)$ , which compresses the full event–level kinematic information into a single likelihood for the entire dataset:
  - (i) Process likelihood. For each selected event  $i$  and each process  $p$  (signal and, separately, each of the background processes) the process-level likelihood is evaluated using Eq. (1):

$$\mathcal{L}_{\text{process}}^p(\kappa_\lambda | \mathbf{x}^i).$$

- (ii) Event likelihood. The previous contributions are combined into the per–event likelihood through the weighted sum for a given event  $i$ :

$$\mathcal{L}_{\text{event}}(\kappa_\lambda | \mathbf{x}^i) = \sum_{p=1}^{n_p} f_p(\kappa_\lambda) \mathcal{L}_{\text{process}}^p(\kappa_\lambda | \mathbf{x}^i), \quad (6)$$

where  $f_p$  denotes the fraction of events in the sample that originates from process  $p$  (with  $\sum_p f_p = 1$ ), fixed here using the theoretically expected signal and background compositions.

- (iii) Kinematic (or sample) likelihood. The kinematic likelihood for the full dataset is then obtained as the product of the event likelihoods:

$$\mathcal{L}_{\text{kin}}(\kappa_\lambda) = \prod_{i=1}^N \mathcal{L}_{\text{event}}(\kappa_\lambda | \mathbf{x}^i), \quad (7)$$

fully encoding the event–level kinematics of the selected sample.

- The *yield likelihood*  $\mathcal{L}_{\text{yield}}(\kappa_\lambda)$ , exploits the strong dependence of the  $gg \rightarrow HH$  production rate on  $\kappa_\lambda$  which is known to vary quadratically due to the interference of the triangle and box diagrams. The yield likelihood follows a Poisson distribution, with parameter  $\mu(\kappa_\lambda) = N_{\text{sig}}(\kappa_\lambda) + N_{\text{bkg}}$ , being the expected event yield, and  $N_{\text{obs}}$  being the observed number of events:

$$\mathcal{L}_{\text{yield}}(\kappa_\lambda) = \frac{\mu(\kappa_\lambda)^{N_{\text{obs}}} e^{-\mu(\kappa_\lambda)}}{N_{\text{obs}}!}. \quad (8)$$

- The *extended likelihood*  $\mathcal{L}_{\text{ext}}$ , defined as the product of the kinematic and yield components,

$$\mathcal{L}_{\text{ext}}(\kappa_\lambda) = \mathcal{L}_{\text{kin}}(\kappa_\lambda) \times \mathcal{L}_{\text{yield}}(\kappa_\lambda), \quad (9)$$

exploiting simultaneously the full event–level kinematic information and the overall dependence of the event yield on  $\kappa_\lambda$ .

## Negative Log-Likelihood

For the statistical extraction of  $\kappa_\lambda$ , it is convenient to work with the negative log-likelihood (NLL), which transforms the product over events in Eq. (9) into a numerically stable sum:

$$\begin{aligned} -\ln \mathcal{L}_{\text{ext}}(\kappa_\lambda) = & - \sum_{i=1}^{N_{\text{obs}}} \ln \mathcal{L}_{\text{event}}(\kappa_\lambda | \mathbf{x}^i) \\ & + \mu(\kappa_\lambda) - N_{\text{obs}} \ln [\mu(\kappa_\lambda)] + C, \end{aligned} \quad (10)$$

where  $C$  is a constant term that does not affect the minimisation of the NLL.

The NLL provides a test statistic whose minimum identifies the best-fit value  $\hat{\kappa}_\lambda$ , while its curvature around the minimum yields the corresponding statistical uncertainty.

This formulation is equivalent to the standard likelihood-ratio approach used in high-energy physics and is well suited for profiling  $\kappa_\lambda$  in large ensembles of pseudo-experiments.

## Likelihood scans and associated histograms

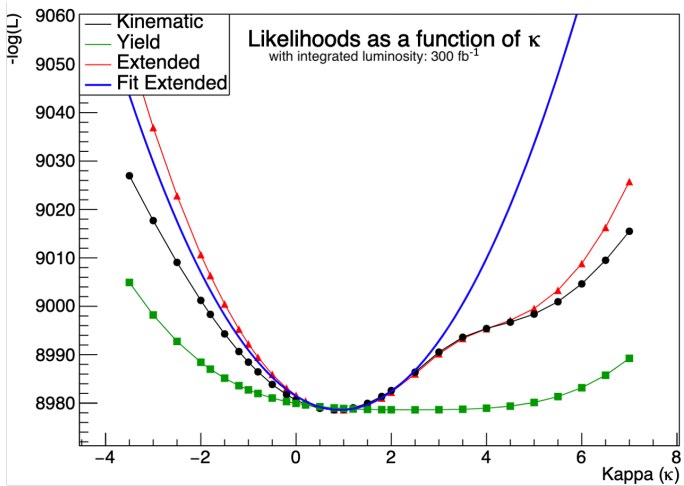


FIG. 3: Likelihood scan for one pseudo-experiment consisting of a combination of NLO signal events ( $\kappa_\lambda = 1$ ) and all main backgrounds, using MEM@NLO.

The graph shows  $-\log \mathcal{L}$  as a function of the hypothesis  $\kappa_\lambda$ . **Black:** kinematic component ( $\mathcal{L}_{\text{kin}}$ ) with offset; **Green:** yield term ( $\mathcal{L}_{\text{yield}}$ ) with offset; **Red:** extended likelihood ( $\mathcal{L}_{\text{ext}}$ ); **Blue:** quadratic fit to  $-\log \mathcal{L}_{\text{ext}}$  around its minimum.

To quantify the performance of the MEM@NLO, an ensemble of 84 independent pseudo-experiments was generated at NLO accuracy, each corresponding to an integrated luminosity of  $300 \text{ fb}^{-1}$  and assuming the Standard Model value  $\kappa_\lambda = 1$ .

Each pseudo-experiment is constructed by fluctuating the expected signal and background yields according to Poisson statistics and by drawing events from the corresponding NLO Monte Carlo samples.

For each pseudo-experiment, the extended likelihood  $\mathcal{L}_{\text{ext}}(\kappa_\lambda)$  is evaluated for a large number of values of  $\kappa_\lambda$ . The result for one of the pseudo-experiments is shown in Fig. 3.

The position of the minimum of the profile  $-\log \mathcal{L}_{\text{ext}}(\kappa_\lambda)$  defines the best-fit value  $\hat{\kappa}_\lambda$ , while the local curvature around the minimum provides an estimate of the statistical uncertainty associated with that pseudo-experiment.

Repeating this procedure over the full set of pseudo-experiments allows one to build distributions of the fitted parameter  $\hat{\kappa}_\lambda$  and the estimation of the corresponding uncertainty.

These distributions are used to assess any bias and the expected statistical uncertainty of the measurement of  $\kappa_\lambda$  using our implementation of the MEM@NLO. The distributions obtained from Monte Carlo pseudo-experiments including signal and all main backgrounds are shown in Fig. 4.

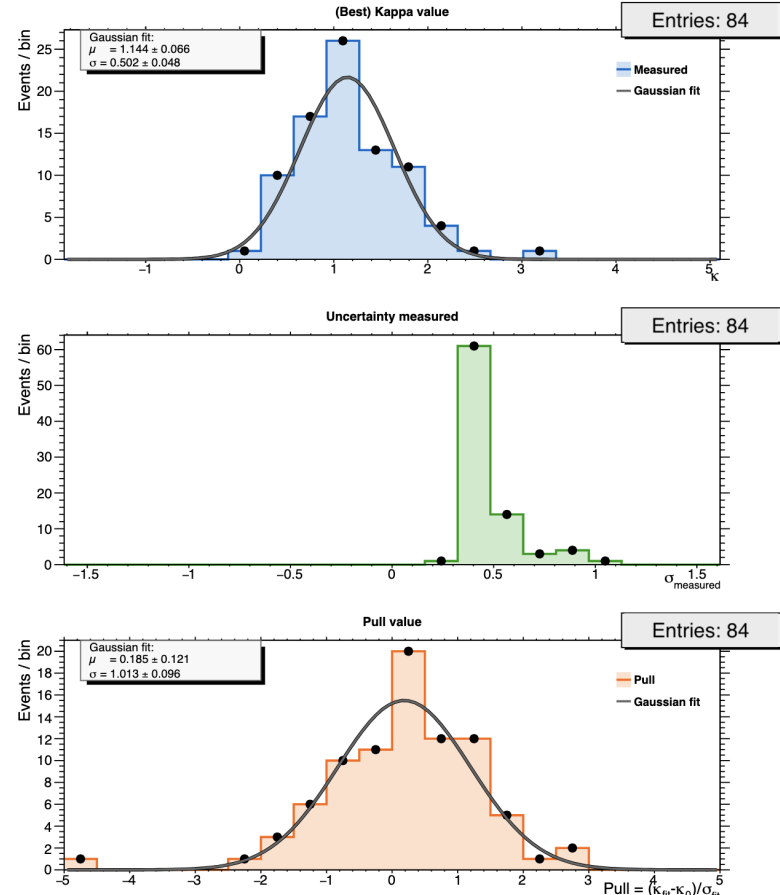


FIG. 4: Histograms of likelihood scan results of pseudo-experiments including signal and all main backgrounds. Top: distribution of the best-fit coupling parameter  $\hat{\kappa}_\lambda$ , with Gaussian fit overlaid. Middle: distribution of the estimated uncertainty  $\sigma_{\text{measured}}$ . Bottom: distribution of the pull values

$$\omega = (\hat{\kappa}_\lambda - \kappa_\lambda^{\text{true}}) / \sigma_{\text{measured}}$$

In addition, we show the distribution of the pull, defined as  $\omega = (\hat{\kappa}_\lambda - \kappa_\lambda^{\text{true}}) / \sigma_{\text{measured}}$ . The pull is used to validate the reliability of the estimated statistical uncertainty. The observed pull distribution is centered around zero and exhibits a width close to unity, indicating that any bias resulting from the implementation of the MEM and the likelihood-based procedure is reasonably small, and that the reported uncertainties are reliable estimates.

## VII. RESULTS

To assess the impact of the different main backgrounds on the expected statistical uncertainty of a measurement of  $\kappa_\lambda$  using the MEM@NLO, we produce and analyse multiple samples with different background compositions: a signal-only sample, samples including each background process individually, and a sample combining all major background sources simultaneously. The results are summarised in Fig. 5 and in Table I. Across all configurations, the injected Standard Model value  $\kappa_\lambda = 1$  is recovered, with acceptable bias (corrections which can be included in a future analysis of collider data). For the analysis of 84 pseudo-experiments, including all main backgrounds,

which offers the most realistic environment, the likelihood fit yields  $\kappa_\lambda = 1.144 \pm 0.502$  where 1.144 represents the mean over all pseudo-experiments, and 0.502 the expected  $1-\sigma$  uncertainty at  $300 \text{ fb}^{-1}$ .

This result demonstrates that the MEM@NLO retains strong sensitivity, even in a challenging background-dominated environment. Another important feature of the MEM@NLO is its ability to remove the mirror solution near  $\kappa_\lambda = 4$ . This secondary solution appears in yield-based analyses because the inclusive  $gg \rightarrow HH$  cross section depends on the interference between the triangle and box diagrams, allowing this second value of  $\kappa_\lambda$  to give the same total rate as the SM. By exploiting the full event-level kinematic information, MEM@NLO breaks this degeneracy and selects only the physical solution.

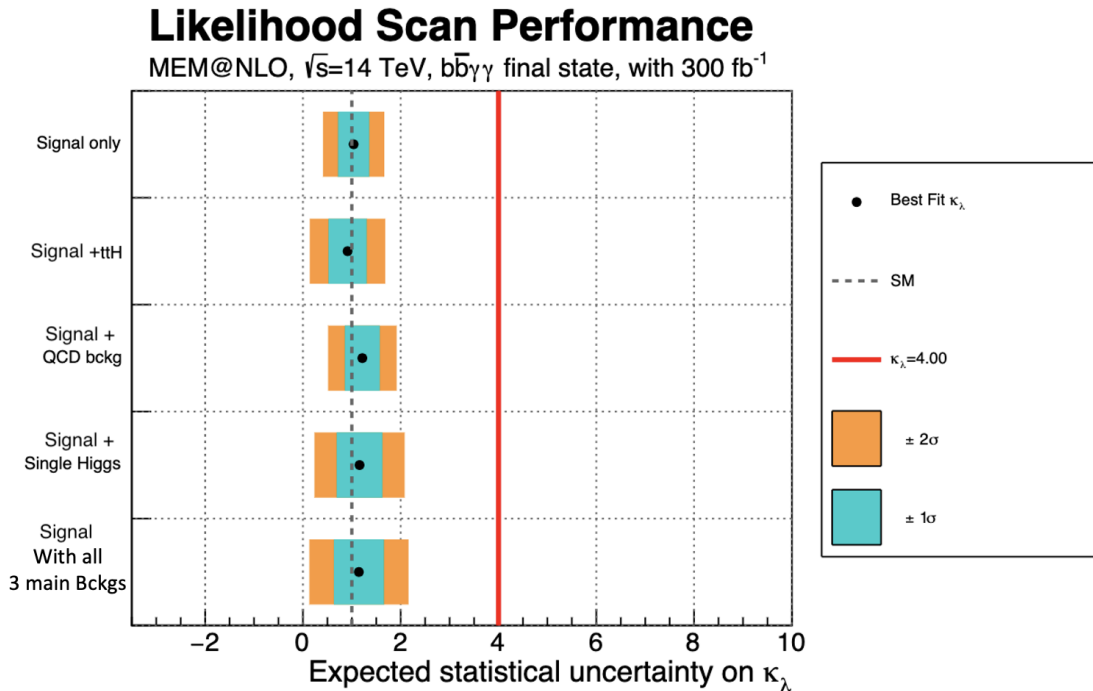


FIG. 5: Summary of likelihood scan performance for MEM@NLO on NLO Monte Carlo pseudo-experiments generated with  $\kappa_\lambda = 1$  in the  $b\bar{b}\gamma\gamma$  final state, with  $300 \text{ fb}^{-1}$ . The black dot marks the mean best-fit value of  $\kappa_\lambda$  for each set of pseudo-experiments, while the bands show the statistical  $\pm 1\sigma$  (turquoise) and  $\pm 2\sigma$  (orange) ranges. The dashed grey line is the SM prediction ( $\kappa_\lambda = 1$ ), and the red vertical line the location of the mirror solution near  $\kappa_\lambda = 4$ .

TABLE I: Summary of likelihood-scan performances for NLO generated events analyzed with MEM@NLO. Each background process listed is included on top of the signal (signal+background). This table corresponds to Fig. 5. Uncertainties in this table reflect the statistical power of the pseudo-experiment sets.

Process	Best fit		Measured uncertainty	Pull distribution	
	$\kappa_{\text{mean}}$	$\sigma_\kappa$		$\omega_{\text{mean}}$	$\sigma_{\text{pull}}$
Signal only	$1.037 \pm 0.012$	$0.309 \pm 0.008$	$0.302 \pm 0.030$	$0.123 \pm 0.039$	$1.020 \pm 0.026$
$t\bar{t}H$	$0.913 \pm 0.042$	$0.441 \pm 0.026$	$0.381 \pm 0.087$	$-0.391 \pm 0.113$	$1.422 \pm 0.092$
QCD ( $b\bar{b}\gamma\gamma$ )	$1.215 \pm 0.040$	$0.354 \pm 0.027$	$0.345 \pm 0.030$	$0.555 \pm 0.126$	$1.023 \pm 0.103$
Single Higgs	$1.158 \pm 0.039$	$0.478 \pm 0.030$	$0.418 \pm 0.088$	$0.296 \pm 0.085$	$1.044 \pm 0.058$
With all backgrounds	<b><math>1.144 \pm 0.066</math></b>	<b><math>0.502 \pm 0.048</math></b>	<b><math>0.485 \pm 0.142</math></b>	<b><math>-0.185 \pm 0.121</math></b>	<b><math>1.013 \pm 0.096</math></b>

### VIII. COMPUTATIONAL COST AND SCALABILITY

As with all applications of the Matrix Element Method, the numerical evaluation of the likelihood involves high-dimensional integrations over the phase space, leading to a substantial computational cost. This feature is intrinsic to any MEM approach, where precision is obtained by integrating over all kinematic configurations compatible with a given reconstructed event (*cf.* Eq. (1)).

The extension of the MEM to next-to-leading order further increases this complexity with the addition of three unresolved radiation degrees of freedom for the real contributions.

The introduction of BLOCK N allows this integration to be performed in a controlled and numerically stable way, but it does not remove the fundamental scaling of the problem with dimensionality.

The dimensionality of the phase-space integrations entering the MEM@NLO evaluation for each signal and background process considered in this study is summarised in Appendix B.

In the present study, the performance of the MoMEMTA framework was optimised as far as possible within its existing design, including careful choices of integration strategies and configuration of the numerical integration algorithms implemented in CUBA [29], the software for integration that is interfaced to MoMEMTA by default. Nevertheless, the computational cost remains significant.

The distribution of the wall-clock time required to evaluate the MEM@NLO likelihood for the signal process<sup>1</sup> is shown in Fig. 6. On average it is 38.8 minutes. Yet for a small fraction of events, the wall-clock was found to reach several hundred minutes, with extreme cases approaching 838 minutes.

Looking forward, several promising directions exist to improve the practical scalability of MEM@NLO. Recent developments in machine-learning-assisted importance sampling and adaptive integration techniques offer the possibility to guide the phase-space exploration toward the most relevant regions, thereby significantly reducing the number of integrand evaluations required. A recent discussion of these approaches can be found *e.g.* in Ref. [30] as well as the references therein [31–39].

In addition, the use of surrogate models to emulate the calculation of the likelihood [40–42] will facilitate systematic studies of theoretical and experimental uncertainties without repeated full re-evaluations.

While these developments are beyond the scope of the

present work, they provide a natural continuation of the MEM@NLO framework introduced here, and will be essential for its application in future high-precision analyses of LHC and HL-LHC data.

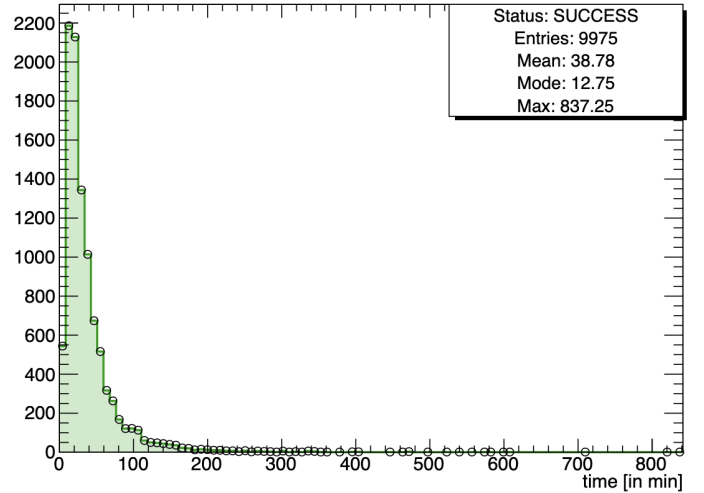


FIG. 6: Wall-clock Time (in minutes) for the calculation of per-event  $\mathcal{L}_{\text{process}}^p$  for an NLO signal sample evaluated for the signal process. The mean, mode and maximum values of the distributions are indicated.

### IX. CONCLUSIONS AND OUTLOOK

We present the first implementation of the MEM at NLO for the extraction of the Higgs boson self-coupling  $\lambda_{3H}$  in Higgs boson pair production in the  $b\bar{b}\gamma\gamma$  channel. A central achievement of this work is the development of BLOCK N, a new integration block specifically designed to treat the additional degrees of freedom associated with real emission contributions at NLO. Its construction required a substantial extension of the existing MoMEMTA formalism and enabled for the first time a consistent NLO treatment, resolving the limitations of previous LO-based approaches.

Validation on simulated samples demonstrates significant improvements in discrimination power and parameter extraction. Ensemble tests confirmed the robustness of the method and its ability to break the mirror solution near  $\kappa_\lambda = 4$ . The method provides a powerful framework for extracting the Higgs self-coupling and can be naturally extended to other analyses or processes.

Future development of this framework could focus on refining the modelling of detector transfer functions and exploring the application of MEM at NLO to a broader range of final states such as  $b\bar{b}\tau^+\tau^-$  or  $bb\bar{b}\bar{b}$ .

As with all applications of the Matrix Element

<sup>1</sup> on a single thread of an AMD EPYC™ 7453 processor, at 2.75 GHz with 28 cores running 56 threads.

Method, the computational cost associated with multidimensional integrations is known to be substantial. Recent developments in machine-learning-based importance sampling and adaptive integration could also offer an interesting direction for future studies, as they could considerably reduce evaluation time while preserving the accuracy of the method.

A further natural extension concerns the systematic treatment of uncertainties. Surrogate model approaches capable of emulating the behaviour of the full likelihood are expected to provide an efficient framework and

enhance the use of MEM at NLO in future analyses.

## ACKNOWLEDGMENTS

We gratefully acknowledge the support of our colleagues at the **IN2P3 Computing Centre** (CC-IN2P3) in Lyon (Villeurbanne) for the reliable and efficient operation of their computing farms. Without this facility, the present study would not have been possible.

- 
- [1] ATLAS Collaboration, *Observation of a new particle in the search for the Standard Model Higgs boson with the ATLAS detector at the LHC*, Physics Letters B **716** (2012) 1-29, doi:[10.1016/j.physletb.2012.08.020](https://doi.org/10.1016/j.physletb.2012.08.020).
- [2] CMS Collaboration, *Observation of a new boson at a mass of 125 GeV with the CMS experiment at the LHC*, Physics Letters B **716** (2012) 30-61, doi:[10.1016/j.physletb.2012.08.021](https://doi.org/10.1016/j.physletb.2012.08.021).
- [3] ATLAS Collaboration, *The ATLAS Experiment at the CERN Large Hadron Collider*, Journal of Instrumentation **3** (2008), doi:[10.1088/1748-0221/3/08/S08003](https://doi.org/10.1088/1748-0221/3/08/S08003).
- [4] CMS Collaboration, *The CMS Experiment at the CERN LHC*, Journal of Instrumentation **3** (2008), doi:[10.1088/1748-0221/3/08/S08004](https://doi.org/10.1088/1748-0221/3/08/S08004).
- [5] ATLAS Collaboration, *Projected sensitivity of searches for Higgs boson pair production in final states with light leptons, taus, and photons with the ATLAS detector at the HL-LHC*, tech. rep., CERN, Geneva (2025), [cds.cern.ch/record/2925675](https://cds.cern.ch/record/2925675).
- [6] ATLAS and CMS Collaborations, *Highlights of the HL-LHC physics projections by ATLAS and CMS* (2025), [arxiv.org/abs/2504.00672](https://arxiv.org/abs/2504.00672).
- [7] M. Reichert, A. Eichhorn, H. Gies, J. M. Pawłowski, T. Plehn, and M. Scherer, *Probing baryogenesis through the Higgs boson self-coupling*, Phys. Rev. D **97** (2018), doi:[10.1103/PhysRevD.97.075008](https://doi.org/10.1103/PhysRevD.97.075008), arXiv:[arxiv.org/abs/1711.00019](https://arxiv.org/abs/1711.00019).
- [8] ATLAS Collaboration, *Combination of searches for Higgs boson pair production in pp collisions at  $\sqrt{s} = 13$  TeV with the ATLAS detector*, Phys. Rev. Lett. **133**, 101801 (2024), doi:[10.1103/PhysRevLett.133.101801](https://doi.org/10.1103/PhysRevLett.133.101801).
- [9] CMS Collaboration, *Combination of searches for non-resonant Higgs boson pair production in proton-proton collisions at  $\sqrt{s} = 13$  TeV*, submitted to Reports on Progress in Physics, arXiv:[2510.07527](https://arxiv.org/abs/2510.07527) (2025).
- [10] ATLAS Collaboration, *Study of Higgs boson pair production in the  $HH \rightarrow b\bar{b}\gamma\gamma$  final state with 308  $\text{fb}^{-1}$  of data collected at  $\sqrt{s} = 13$  TeV and 13.6 TeV by the ATLAS experiment*, arXiv:[arxiv.org/abs/2507.03495](https://arxiv.org/abs/2507.03495) (2025).
- [11] K. Kondo, *Dynamical Likelihood Method for Reconstruction of Events with Missing Momentum. I. Method and Toy Models*, J. Phys. Soc. Jap. **57**, no. 12, 4126-4140 (1988), doi:[10.1143/JPSJ.57.4126](https://doi.org/10.1143/JPSJ.57.4126).
- [12] K. Kondo, *Dynamical Likelihood Method for Reconstruction of Events with Missing Momentum. II. Mass Spectra for 2  $\rightarrow$  2 Processes*, J. Phys. Soc. Jap. **60**, no. 3, 836-844 (1991), doi:[10.1143/JPSJ.60.836](https://doi.org/10.1143/JPSJ.60.836).
- [13] DØ Collaboration, *Measurement of the Top Quark Mass Using Dilepton Events*, Phys. Rev. Lett. **80**, 2063-2068 (1998), doi:[10.1103/PhysRevLett.80.2063](https://doi.org/10.1103/PhysRevLett.80.2063), arXiv:[arxiv.org/abs/hep-ex/9706014](https://arxiv.org/abs/hep-ex/9706014).
- [14] F. Canelli, *Helicity of the W boson in single-lepton  $t\bar{t}$  events*, Ph.D. thesis, Rochester University (2003), doi:[10.1142/S0217751X03016689](https://doi.org/10.1142/S0217751X03016689).
- [15] DØ Collaboration, *A Precision Measurement of the Mass of the Top Quark*, Nature **429**, 638 (2004), doi:[10.1038/nature02589](https://doi.org/10.1038/nature02589), arXiv:[arxiv.org/abs/hep-ex/0406031](https://arxiv.org/abs/hep-ex/0406031).
- [16] J. Alwall, A. Freitas and O. Mattelaer, *Matrix element method and QCD radiation*, Phys. Rev. D **83**, 074010 (2011), doi:[10.1103/PhysRevD.83.074010](https://doi.org/10.1103/PhysRevD.83.074010), arXiv:[arxiv.org/abs/1010.2263](https://arxiv.org/abs/1010.2263) (2010).
- [17] J. M. Campbell, W. T. Giele, and C. Williams, *The Matrix Element Method at Next-to-Leading Order*, doi:[10.1007/JHEP11\(2012\)043](https://doi.org/10.1007/JHEP11(2012)043), arXiv:[arxiv.org/abs/1204.4424](https://arxiv.org/abs/1204.4424) (2012).
- [18] T. Martini and P. Uwer, *The Matrix Element Method at next-to-leading order QCD for hadronic collisions: single top-quark production at the LHC as an example application*, JHEP **05**, 141 (2018), doi:[10.1007/JHEP05\(2018\)141](https://doi.org/10.1007/JHEP05(2018)141).
- [19] T. Martini, T. Nuraliyev and P. Uwer, *Determination of the top-quark mass from top-quark pair events with the matrix element method at next-to-leading order: Potential and prospects*, arXiv:[arxiv.org/abs/2301.03280](https://arxiv.org/abs/2301.03280) [hep-ph] (2023).
- [20] M. Tartarin, *Measurement of the Higgs self-coupling using the Matrix Element Method at Next-to-Leading Order (NLO) in the  $gg \rightarrow HH \rightarrow b\bar{b}\gamma\gamma$  channel for the ATLAS experiment at the LHC*, Ph.D. thesis, Université de Toulouse (2025), doi:[10.17181/8hbdr-mgg27](https://doi.org/10.17181/8hbdr-mgg27).
- [21] F. Eble and J. Stark, *Prospective study for the development of an analysis to measure the tri-linear Higgs coupling using the Matrix Element Method with the ATLAS experiment at the HL-LHC*, Master thesis, KTH Royal Institute of Technology (2020), <https://urn.kb.se/resolve?urn=urn:nbn:se:kth:diva-291100>.
- [22] S. Wertz et al., *MoMEMta: A modular matrix element method framework*, Eur. Phys. J. C **77** (2017) 708.
- [23] S. Alioli, P. Nason, C. Oleari and E. Re, *A general framework for implementing NLO calculations in shower Monte Carlo programs: the POWHEG BOX*, J. High Energ. Phys. **2010** (6), 43 (2010), doi:[10.1007/JHEP06\(2010\)043](https://doi.org/10.1007/JHEP06(2010)043).

- [24] G. Heinrich et al., *NLO predictions for Higgs boson pair production with full top quark mass dependence matched to parton showers*, *JHEP* **08**, 088 (2017), doi:[10.1007/JHEP08\(2017\)088](https://doi.org/10.1007/JHEP08(2017)088), arXiv:[1703.09252](https://arxiv.org/abs/1703.09252).
- [25] G. Heinrich et al., *Probing the trilinear Higgs boson coupling in di-Higgs production at NLO QCD including parton shower effects*, *JHEP* **06**, 066 (2019), doi:[10.1007/JHEP06\(2019\)066](https://doi.org/10.1007/JHEP06(2019)066), arXiv:[1903.08137](https://arxiv.org/abs/1903.08137).
- [26] T. Sjöstrand et al., *An Introduction to PYTHIA 8.2*, *Comput. Phys. Commun.* **191**, 159-177 (2015), doi:[10.1016/j.cpc.2015.01.024](https://doi.org/10.1016/j.cpc.2015.01.024), arXiv:[1410.3012](https://arxiv.org/abs/1410.3012).
- [27] M. Tartarin and J. Stark, *MEM@NLO ggHH auxiliary material and code (GitLab repository)*, [https://gitlab.com/mtartarin/phd\\_share](https://gitlab.com/mtartarin/phd_share).
- [28] J. Alwall et al., *The automated computation of tree-level and next-to-leading order differential cross sections, and their matching to parton shower simulations*, *J. High Energ. Phys.* **2014** (7), 79 (2014), doi:[10.1007/JHEP07\(2014\)079](https://doi.org/10.1007/JHEP07(2014)079), arXiv:[1405.0301](https://arxiv.org/abs/1405.0301).
- [29] T. Hahn, *CUBA — A Library for Multidimensional Numerical Integration*, doi:[10.1016/j.cpc.2007.03.006](https://doi.org/10.1016/j.cpc.2007.03.006), arXiv:[hep-ph/0404043](https://arxiv.org/abs/hep-ph/0404043) [hep-ph] (2004).
- [30] M. Ubiali, *Modern machine learning and particle physics phenomenology at the LHC*, summary talk given at *EuCAIFCon 2025 (European AI for Fundamental Physics Conference)*, Cagliari, Italy, 17 June 2025, <https://agenda.infn.it/event/43565/contributions/268339/>.
- [31] F. Bishara and M. Montull, *(Machine) Learning Amplitudes for Faster Event Generation*, *Phys. Rev. D* **107**, L071901 (2023), doi:[10.1103/PhysRevD.107.L071901](https://doi.org/10.1103/PhysRevD.107.L071901), arXiv:[1912.11055](https://arxiv.org/abs/1912.11055) [hep-ph] (2019).
- [32] S. Badger and J. Bullock, *Using Neural Networks for Efficient Evaluation of High Multiplicity Scattering Amplitudes*, doi:[10.1007/JHEP06\(2020\)114](https://doi.org/10.1007/JHEP06(2020)114), arXiv:[2002.07516](https://arxiv.org/abs/2002.07516) [hep-ph] (2020).
- [33] A. Buckley, A. Kvellestad, Å. Raklev, P. Scott, J. V. Sparre, J. Van den Abeele and I. A. Vazquez-Holm, *Xsec: the Cross-Section Evaluation Code*, doi:[10.1140/epjc/s10052-020-08635-y](https://doi.org/10.1140/epjc/s10052-020-08635-y), arXiv:[2006.16273](https://arxiv.org/abs/2006.16273) [hep-ph, hep-ex] (2020).
- [34] D. L. B. Sombillo, Y. Ikeda, T. Sato and A. Hosaka, *Model Independent Analysis of Coupled-Channel Scattering: A Deep Learning Approach*, *Phys. Rev. D* **104**, 036001 (2021), doi:[10.1103/PhysRevD.104.036001](https://doi.org/10.1103/PhysRevD.104.036001), arXiv:[2105.04898](https://arxiv.org/abs/2105.04898).
- [35] J. Aylett-Bullock, S. Badger and R. Moodie, *Optimising Simulations for Diphoton Production at Hadron Colliders Using Amplitude Neural Networks*, doi:[10.1007/JHEP08\(2021\)066](https://doi.org/10.1007/JHEP08(2021)066), arXiv:[2106.09474](https://arxiv.org/abs/2106.09474) [hep-ph] (2021).
- [36] K. Danziger, T. Janßen, S. Schumann and F. Siegert, *Accelerating Monte Carlo Event Generation — Rejection Sampling Using Neural Network Event-Weight Estimates*, doi:[10.21468/SciPostPhys.12.5.164](https://doi.org/10.21468/SciPostPhys.12.5.164), arXiv:[2109.11964](https://arxiv.org/abs/2109.11964) [hep-ph, hep-ex] (2021).
- [37] A. Alnuqaydan, S. Gleyzer and H. Prosper, *SYMBA: Symbolic Computation of Squared Amplitudes in High Energy Physics with Machine Learning*, doi:[10.1088/2632-2153/acb2b2](https://doi.org/10.1088/2632-2153/acb2b2), arXiv:[2206.08901](https://arxiv.org/abs/2206.08901) [hep-ph, cs.LG] (2022).
- [38] D. Maître and H. Truong, *One-Loop Matrix Element Emulation with Factorisation Awareness*, doi:[10.1007/JHEP05\(2023\)159](https://doi.org/10.1007/JHEP05(2023)159), arXiv:[2302.04005](https://arxiv.org/abs/2302.04005) [hep-ph] (2023).
- [39] T. Janßen, D. Maître, S. Schumann, F. Siegert and H. Truong, *Unweighting Multijet Event Generation Using Factorisation-Aware Neural Networks*, doi:[10.21468/SciPostPhys.15.3.107](https://doi.org/10.21468/SciPostPhys.15.3.107), arXiv:[2301.13562](https://arxiv.org/abs/2301.13562) [hep-ph, hep-ex] (2023).
- [40] P. Chang, S. Gleyzer, M. Neubauer and D. Zhong, *Sustainable Matrix Element Method through Deep Learning*, Zenodo (Sept., 2017), doi:[10.5281/zenodo.4008241](https://doi.org/10.5281/zenodo.4008241).
- [41] F. Bury and C. Delaere, *Matrix Element Regression with Deep Neural Networks — breaking the CPU barrier*, doi:[10.1007/JHEP04\(2021\)020](https://doi.org/10.1007/JHEP04(2021)020), arXiv:[2008.10949](https://arxiv.org/abs/2008.10949) [hep-ex, hep-ph] (2020).
- [42] M. Feickert, M. Katare, M. Neubauer and A. Roy, *Deep Learning for the Matrix Element Method*, doi:[10.22323/1.414.0246](https://doi.org/10.22323/1.414.0246), arXiv:[2211.11910](https://arxiv.org/abs/2211.11910) [hep-ex, hep-ph] (2022).

## Appendix A: Validation of Block N

The introduction of BLOCK N constitutes a central extension of the MoMEMTA formalism at NLO, enabling for the first time the treatment of real-emission contributions within the Matrix Element Method. Because this construction is not covered by existing implementations, a dedicated validation procedure was required.

### Validation strategy

The validation is based on a direct and physically motivated comparison between the behaviour of the MEM integrand constructed with BLOCK N and the kinematic properties of real-emission events generated at NLO.

The longitudinal momentum of the unresolved real-emission parton,  $p_z^{\text{rad}}$ , is a natural probe of the Block N construction, as it is the only remaining integration variable associated with the extra parton after enforcing four-momentum conservation.

For a large sample of NLO signal events generated with POWHEG-BOX-V2, the distribution of  $p_z^{\text{rad}}$  is compared to the behaviour of the MEM integrand evaluated at the same phase-space points using BLOCK N. This comparison allows one to assess whether the MEM integrand correctly reproduces the physical distribution of the unresolved radiation.

### Progressive inclusion of MEM ingredients

To isolate the impact of each ingredient entering the MEM@NLO construction, the validation is performed in successive steps of increasing complexity, shown in Fig. 7:

- Real matrix element only [Fig. 7(a,b)]: the squared real-emission matrix element is evaluated as a function of  $p_z^{\text{rad}}$ , without parton distribution functions or Jacobian factors.
- Real matrix element with PDFs [Fig. 7(c,d)]: the same quantity is weighted by the initial-state parton distribution functions, introducing the dependence on the Bjorken- $x$  momentum fractions.
- Full MEM integrand [Fig. 7(e,f)]: the complete integrand is constructed by combining the real matrix element, the parton distribution functions, and the full Jacobian associated with the BLOCK N transformation and the phase-space measure.

At each stage, the mean of the quantity under study (real matrix element, ..., full MEM integrand) is shown in bins of  $p_z^{\text{rad}}$ , and compared to the distribution of  $p_z^{\text{rad}}$  in red from the NLO Monte Carlo events. All distributions are normalised to unity to facilitate a direct comparison of their shapes.

### Results and interpretation

The comparison shows that neither the real matrix element alone nor its PDF-weighted form is sufficient to reproduce the physical  $p_z^{\text{rad}}$  distribution.

In both cases, sizable distortions appear, indicating that large regions of the integration domain are improperly weighted.

Only after the inclusion of the full Jacobian associated with this configuration (partially derived in section IV for the BLOCK N contribution only) does the MEM integrand accurately follow the Monte Carlo distribution over the full range of  $p_z^{\text{rad}}$ .

This validation confirms that BLOCK N provides a physically coherent treatment of real-emission phase space within the MEM@NLO framework. It ensures that unresolved radiation is integrated consistently, without biasing the likelihood or distorting its kinematic dependence, thereby enabling reliable NLO-accurate applications of the Matrix Element Method.

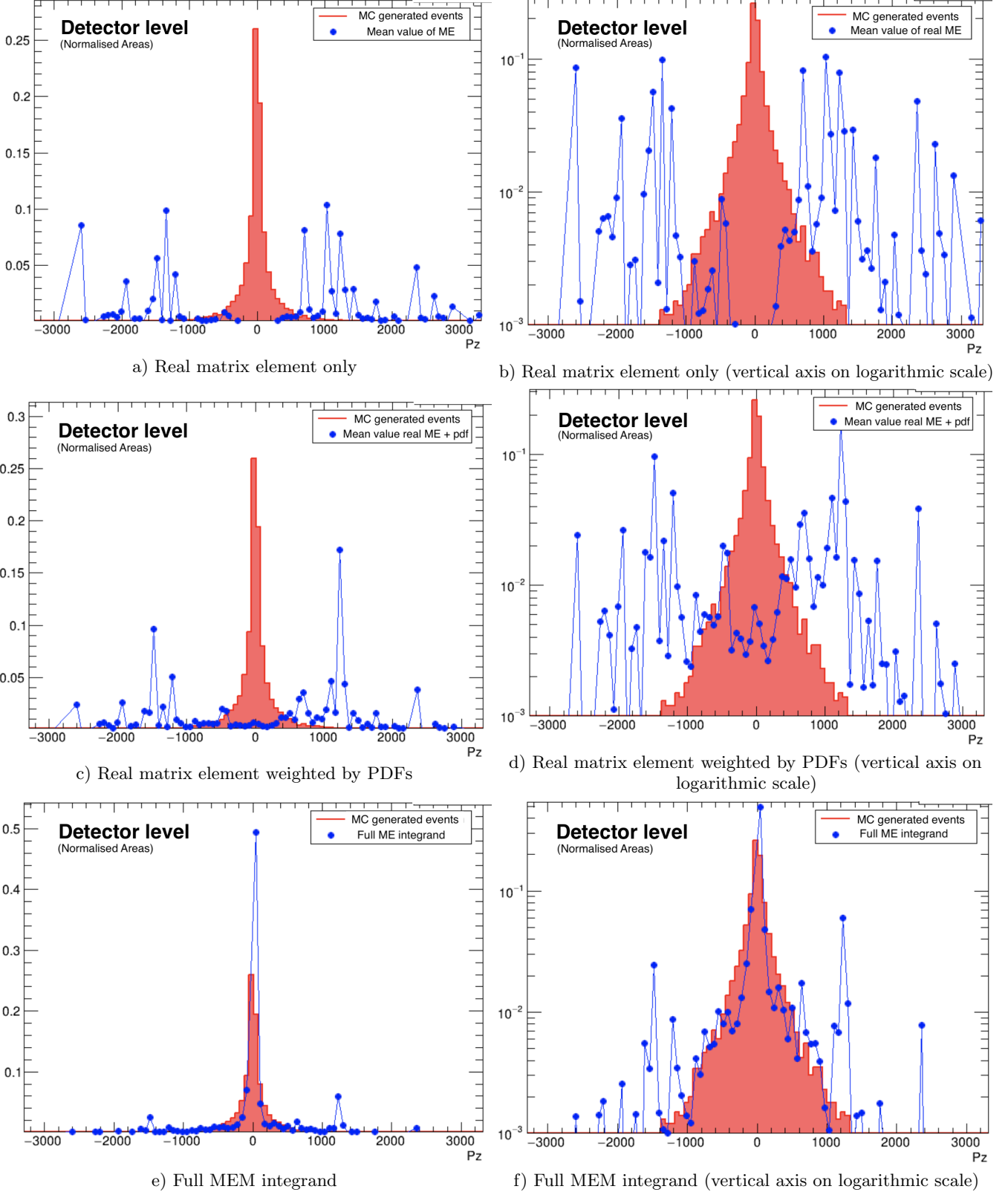


FIG. 7: Validation of the BLOCK N construction using the longitudinal momentum of the unresolved real-emission parton  $p_z^{\text{rad}}$ . Panels show the distribution of  $p_z^{\text{rad}}$  obtained from NLO Monte Carlo events (red) compared to the mean value of the MEM integrand evaluated with BLOCK N (blue), with all distributions normalised to unity. Results are shown for increasing levels of complexity: (a,b) real matrix element only, (c,d) real matrix element weighted by parton distribution functions, and (e,f) full MEM integrand including the Block N Jacobian. Right panels use a logarithmic vertical axis for the vertical axis.

## Appendix B: Degrees of Freedom and Integration Dimensionality

For a given reconstructed final state, the number of integration variables depends on the underlying hard-scattering process, the decay topology, and the perturbative order considered.

Table II summarises the effective number of integration degrees of freedom used in this analysis for the main signal and background processes, at both leading order (LO) and next-to-leading order (NLO). The specific choice of integration variables is not unique, but the choices listed here were found to provide stable and efficient numerical convergence.

Following standard practice in MEM analyses, the resolution on the direction of final-state objects in momentum space is neglected in the calculation of  $\mathcal{L}_{\text{process}}$  (*i.e.* the measured directions are used to evaluate the parton-level matrix element), which substantially reduces the number of integration variables.

Integration variables mainly correspond to the energies  $E$  of reconstructed final-state objects (photons  $\gamma$ ,

$b$  jets), and the Bjorken- $x$  momentum fractions ( $q_1, q_2$ ) for the initial-state partons. Intermediate resonance widths may be neglected, leading to a further reduction of the dimensionality of the numerical integration (this reduction is indicated by an arrow ‘ $\rightarrow$ ’ in the *Integration dimension* column of Table II).

At NLO, real-emission contributions introduce additional degrees of freedom associated with an unresolved parton. These are denoted by the superscript ‘rad’ and correspond to momentum components of the extra radiation that are fully integrated over in the MEM likelihood. The treatment of these additional degrees of freedom is enabled either by the BLOCK N module described in the main text, or by the EXTRARADIATION\_3DOF module.

We created the EXTRARADIATION\_3DOF module to introduce three additional independent integration dimensions which can be parameterized either in Cartesian coordinates ( $p_x, p_y, p_z$ ) or in cylindrical phase space ( $p_T, \phi, E$ ) depending on the user needs. This specific module has been designed for processes where the presence of invisible particles at LO (*e.g.*  $t\bar{t}H$ ) already force the choice of main (and secondary) blocks and consequently forbids the use of BLOCK N.

Process	Integration dimension	Representative integration variables
$gg \rightarrow HH @ \text{LO}$	<b>2</b> ( $\rightarrow 0$ )	( $H$ width), $\gamma_{1,E}$
$t\bar{t}H @ \text{LO}$	<b>9</b> ( $\rightarrow 6$ )	( $H$ width, $\text{top}_1$ width, $\text{top}_2$ width), permutation of $(b_3, b_4)$ , $\gamma_{1,E}, b_{3,E}, b_{4,E}, q_1, q_2$
QCD $b\bar{b}\gamma\gamma @ \text{LO}$	<b>2</b>	$\gamma_{1,E}, \gamma_{2,E}$
Single Higgs @ LO	<b>2</b>	( $H$ width), $\gamma_{1,E}$
$gg \rightarrow HH @ \text{NLO (real)}$	5 ( $\rightarrow 3$ )	( $H_1$ width, $H_2$ width), $\gamma_{1,E}, b_{3,E}, p_z^{\text{rad}}$
$t\bar{t}H @ \text{NLO (real)}$	12 ( $\rightarrow 9$ )	LO variables + $p_T^{\text{rad}}, \phi^{\text{rad}}, E^{\text{rad}}$
QCD $b\bar{b}\gamma\gamma @ \text{NLO (real)}$	<b>5</b>	$\gamma_{1,E}, \gamma_{2,E}, b_{3,E}, b_{4,E}, p_z^{\text{rad}}$
Single Higgs @ NLO (real)	<b>5</b>	( $H$ width), $\gamma_{1,E}, b_{3,E}, b_{4,E}, p_z^{\text{rad}}$

TABLE II: Summary of integration dimensions and choices of integration variables used in the MEM calculation for each LO and NLO processes. Values in parentheses indicate the reduced dimensionality obtained after constraining the width of off-shell particles (from Breit-Wigner propagators to the Narrow width approximation).